J Mater Sci (2013) 48:2745–2760
DOI 10.1007/s10853-012-6895-z

High performance Bi_2Te_3 nanocomposites prepared by single-element-melt-spinning spark-plasma sintering

Wenjie Xie · Shanyu Wang · Song Zhu · Jian He · Xinfeng Tang · Qingjie Zhang · Terry M. Tritt

Received: 22 May 2012 / Accepted: 12 September 2012 / Published online: 22 September 2012

Abstract The last decade has witnessed nanocomposites becoming a new paradigm in the field of thermoelectric (TE) research. At its core is to prepare high performance TE nanocomposites, both *p*- and *n*-type, in a time and energy efficient way. To this end, we in this article summarize our recent effort and results on both *p*- and *n*-type Bi_2Te_3-based nanocomposites prepared by a unique single-element-melt-spinning spark-plasma sintering procedure. The results of transport measurements, scanning and transmission electronic microscopy, and small angle neutron scattering have proved essential in order to establish the correlation between the nanostructures and the TE performance of the materials. Interestingly, we find that in situ formed nanocrystals with coherent boundaries are the key nanostructures responsible for the significantly improved TE performance of *p*-type Bi_2Te_3 nanocomposites whereas similar nanostructures turn out to be less effective for *n*-type Bi_2Te_3 nanocomposites. We also discuss the alternative strategies to further improve the TE performance of *n*-type Bi_2Te_3 materials via nanostructuring processes.

W. Xie (✉) · S. Wang · X. Tang (✉) · Q. Zhang
State Key Laboratory of Advanced Technology for Materials Synthesis and Processing, Wuhan University of Technology, Wuhan 430070, People's Republic of China
e-mail: michaelwhwut@gmail.com

X. Tang
e-mail: tangxf@whut.edu.cn

W. Xie
Empa, Swiss Federal Laboratories for Materials Science and Technology, 8600 Dubendorf, Switzerland
e-mail:wenjie.xie@empa.ch

S. Zhu · J. He · T. M. Tritt
Department of Physics & Astronomy, Clemson University, Clemson, SC 29634-0978, USA

Introduction

It has been nearly two centuries since Seebeck [1] discovered the thermoelectric (TE) effect named in his honor, and more than half a century since Ioffe [2] initiated modern TE studies of semiconductors in the 1950s. TE research is materials oriented and performance gauged; the ultimate goal is to develop higher performance materials in order to attain higher efficiency of thermal-to-electrical energy conversion. The performance of TE material is assessed by the dimensionless figure of merit, $ZT = \sigma\alpha^2/\kappa T = \alpha^2/\rho\kappa T$, where σ is the electrical conductivity (ρ the electrical resistivity), α the Seebeck coefficient, κ the total thermal conductivity (in the simplest case, $\kappa = \kappa_L + \kappa_e$, where κ_L and κ_e are the lattice and electronic contributions, respectively), and T the temperature in Kelvin. An ideal TE material should simultaneously have high σ, large α (in magnitude), and low κ, i.e., an "electron crystal phonon glass" material as dubbed succinctly by Slack [3]. While there is no known limit to the maximum ZT value, most state-of-the-art TE materials have a $ZT \sim 1$–2 because σ, α, κ are interdependent: thus optimizing one quantity often adversely affects the other.

As of date high performance bulk TE materials such as Bi_2Te_3 [4–6], PbTe [7–9], and SiGe [10–12] have found applications in TE cooling and power generation. For convenience, we hereafter call these bulk materials "traditional TE materials" to distinguish from the TE nanocomposites. Currently the strategy of TE study is basically two-fold: (1) to pursue higher ZT in traditional TE materials via nanostructuring process; and (2) to explore new high ZT bulk materials, to name a few, half-Heuslers [13–17], filled skutterudites [18–22], Zintl phases [23–27], and filled clathrates [28–31]. The study reviewed herein is in line with the first strategy and focused on Bi_2Te_3 compounds.

Bi_2Te_3 compounds have been the most widely used traditional TE material in the temperature range of 200–400 K for a few decades. To make Bi_2Te_3-based devices more competitive in large-scale and high-power commercial applications, the *ZT* of Bi_2Te_3 materials must be improved significantly. Furthermore, in view of that Bi_2Te_3 compounds are commercialized and the parasitic losses and device issues related to these Bi_2Te_3 compounds are well understood in the TE device industry for years, then such improvement of *ZT* would much more easily transit into the production of TE devices than an entirely new material with an even higher *ZT*. The challenge is how to achieve the improvement of *ZT* in a time and energy efficient way.

Per the definition of *ZT*, the options are: (i) to further enhance the power factor ($PF = \sigma\alpha^2 = \alpha^2/\rho$); (ii) to reduce the lattice thermal conductivity, and/or (iii) a combination of (i) and (ii). For example, alloying is a popular option in line with (iii). Ioffe early proposed TE performance could be remarkably enhanced by forming solid solutions with isoelectronic atoms. On the one hand, the electronegativity difference between the isoelectronic atoms allows for optimizing the electronic band structure (band gap, effective mass, and carrier concentrations, etc.) and thus improving the power factor. On the other hand, the isoelectronic alloys introduce short-range defects that scatter phonons more effectively than charge carriers at elevated temperatures due to mass field and strain field fluctuations. This idea has been implemented in Bi_2Te_3 compounds with great success [32]: by substituting Sb at the Bi site and Se at the Te site, and *ZT* values $\sim$1.0 and 0.9 were attained near 330 K in *p*-type $Bi_{0.5}Sb_{1.5}Te_3$ and *n*-type $Bi_2Te_{2.85}Se_{0.15}$ solid solutions, respectively. However, it is widely accepted that the room for further optimization via doping has reached its limit, novel approaches are needed.

In 1993, Hicks and Dresselhaus [33] proposed the technical merits of low-dimensional nanostructured TE materials. The advantages are two-fold: first, quantum confinement effect of charge carriers can increase the Seebeck coefficient without degrading the electrical conductivity much; second, the lattice thermal conductivity can be significantly reduced owing to strong phonon scattering on the boundaries or interfaces. As such, the limitation imposed by the interdependence of (σ, ρ, and κ) can be somewhat eased. In this spirit, the *ZT* of Bi_2Te_3/Sb_2Te_3

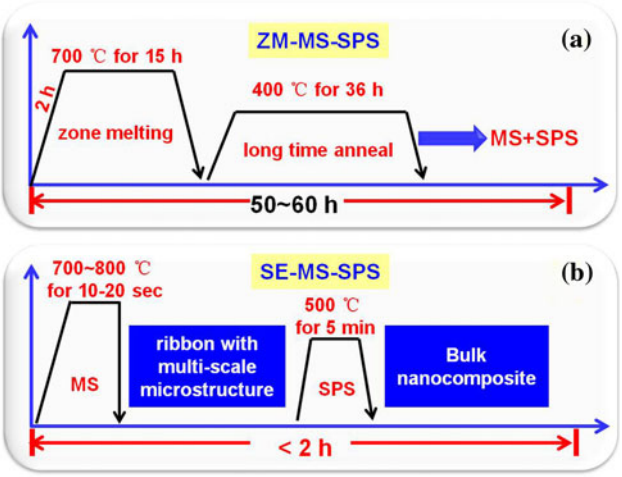

Fig. 1 Time consumption in **a** ZM-MS–SPS and **b** SE-MS–SPS processes

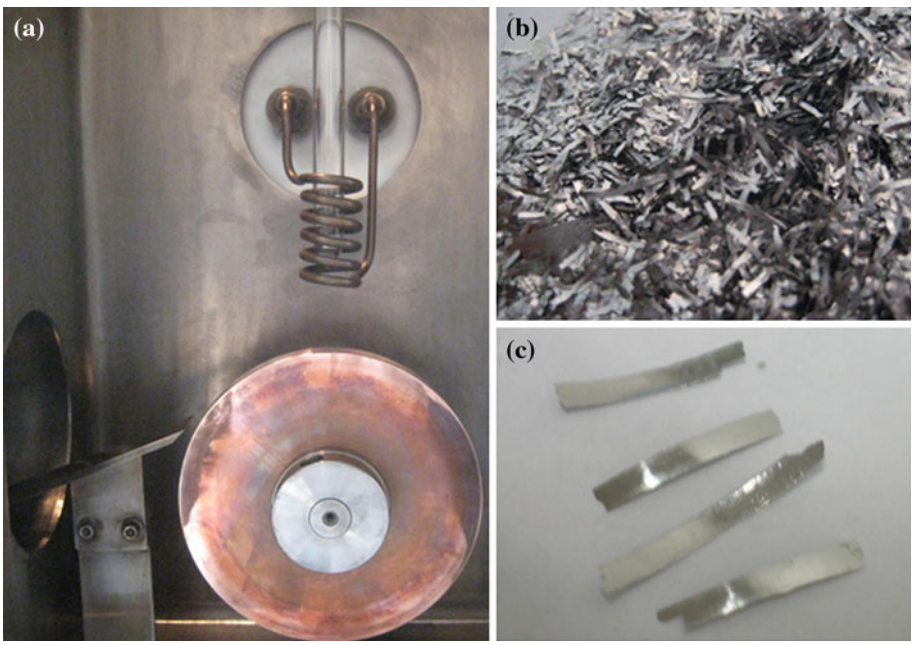

Fig. 2 **a** Melt-spinning system, **b** Melt-spun Bi_2Te_3 ribbons, and **c** *four ribbons* show the contact surface (convex) and free surface (concave)

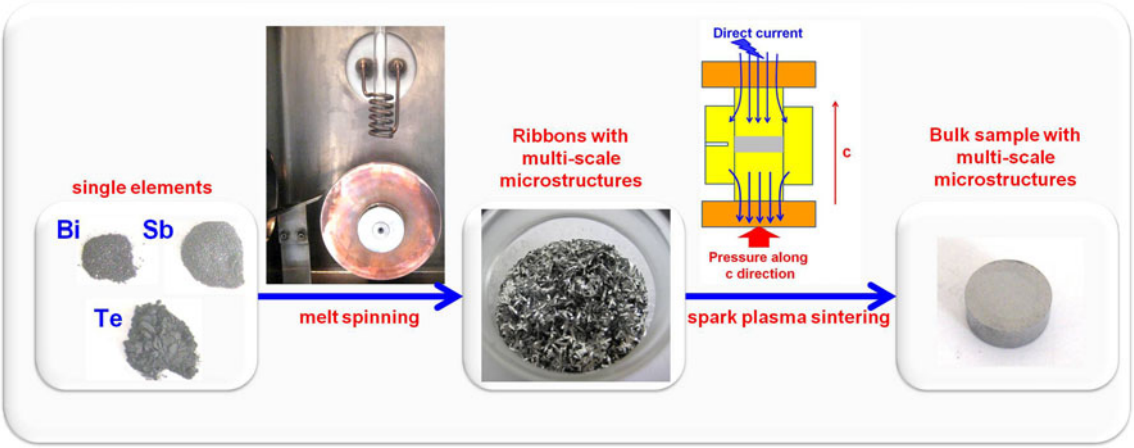

Fig. 3 SE-MS–SPS process

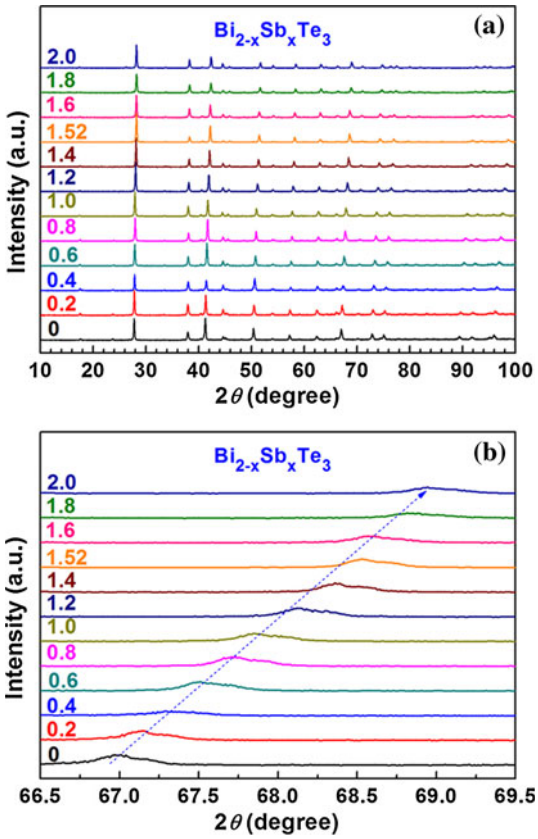

Fig. 4 XRD patterns of SE-MS-$Bi_{2-x}Sb_xTe_3$ ribbons: **a** full pattern; **b** magnification of pattern shown in the range of 66.5–69.5°

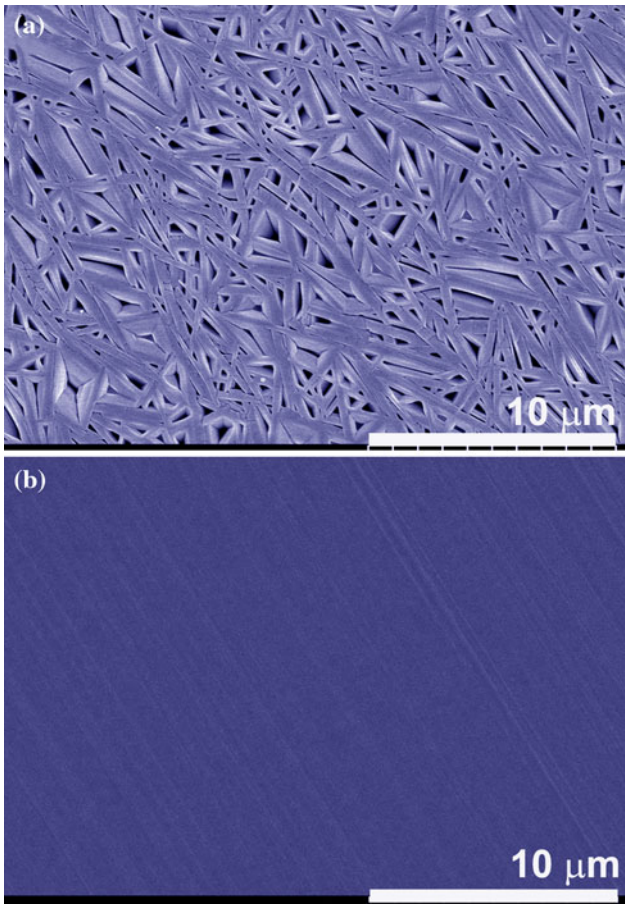

Fig. 5 FESEM images of SE-MS-Bi_2Te_3 ribbon sample: **a** free surface and **b** contact surface

superlattice thin film prepared by molecular beam epitaxial method (MBE) reached unprecedented $ZT \sim 2.4$ at 300 K [34]. While this breakthrough is proof of principle and promising, the complex preparation techniques and high cost limit their broader application. It is thus desirable to combine the higher performance of nanostructured TE materials and the low cost high yield of traditional bulk TE materials, which leads to the new paradigm of nanocomposite TE materials.

Over the past decade, nanocomposite TE materials become a new paradigm in the field of TE research. In

Table 1 The nominal composition and EDS results of SE-MS-$Bi_{2-x}Sb_xTe_3$ ribbons including contact surface and free surface

x	Nominal composition	EDS composition on contact surface	EDS composition on free surface
0	Bi_2Te_3	$Bi_{40.75}Te_{59.25}$	$Bi_{40.36}Te_{59.64}$
0.2	$Bi_{1.8}Sb_{0.2}Te_3$	$Bi_{36.86}Sb_{3.73}Te_{59.41}$	$Bi_{37.55}Sb_{2.92}Te_{59.53}$
0.4	$Bi_{1.6}Sb_{0.4}Te_3$	$Bi_{32.86}Sb_{7.73}Te_{59.41}$	$Bi_{33.86}Sb_{6.73}Te_{59.41}$
0.6	$Bi_{1.4}Sb_{0.6}Te_3$	$Bi_{27.34}Sb_{12.96}Te_{59.71}$	$Bi_{28.15}Sb_{11.94}Te_{59.91}$
0.8	$Bi_{1.2}Sb_{0.8}Te_3$	$Bi_{25.39}Sb_{14.19}Te_{60.42}$	$Bi_{24.76}Sb_{15.44}Te_{59.80}$
1.0	$Bi_{1.0}Sb_{1.0}Te_3$	$Bi_{19.14}Sb_{21.17}Te_{59.69}$	$Bi_{19.95}Sb_{20.66}Te_{59.39}$
1.2	$Bi_{0.8}Sb_{1.2}Te_3$	$Bi_{15.64}Sb_{24.87}Te_{59.49}$	$Bi_{17.05}Sb_{23.66}Te_{59.39}$
1.4	$Bi_{0.6}Sb_{1.4}Te_3$	$Bi_{12.23}Sb_{28.35}Te_{59.42}$	$Bi_{11.96}Sb_{28.58}Te_{59.46}$
1.52	$Bi_{0.48}Sb_{1.52}Te_3$	$Bi_{9.52}Sb_{31.15}Te_{59.33}$	$Bi_{10.31}Sb_{30.32}Te_{58.34}$
1.6	$Bi_{0.4}Sb_{1.6}Te_3$	$Bi_{8.41}Sb_{33.58}Te_{58.01}$	$Bi_{8.37}Sb_{31.91}Te_{59.72}$
1.8	$Bi_{0.2}Sb_{1.8}Te_3$	$Bi_{2.74}Sb_{37.22}Te_{60.04}$	$Bi_{4.13}Sb_{34.99}Te_{60.88}$
2.0	Sb_2Te_3	$Sb_{41.29}Te_{58.71}$	$Sb_{41.95}Te_{58.05}$

nanocomposite TE materials, the characteristic length scale of at least one constituent is on the nanometer scale; the resulting classical and quantum size effects help ease the interdependence of those properties. Many nanocomposites achieved higher *ZT* than their traditional bulk counterparts, to name a few, PbTe-based alloys [35–38], filled $CoSb_3$ [39–43], half-Heusler [44–49], SiGe [50, 51], and Bi_2Te_3-based compounds [52–61].

This review serves to provide a summary of our recent research efforts on both *p*- and *n*-type Bi_2Te_3 nanocomposites prepared by a single-element-melt-spinning spark-plasma sintering (SE-MS–SPS) procedure. In particular, the MS–SPS technique was first introduced by us to prepare Bi_2Te_3-based TE nanocomposites [62]. This article is organized as follows: we will first introduce the MS–SPS process as well as SE-MS–SPS, in view of the classical zone melting (ZM) method of preparing traditional Bi_2Te_3 bulk materials. Then we present the results of microscopy study and TE properties of *p*- and *n*-type Bi_2Te_3 nanocomposites prepared by SE-MS–SPS procedure, a greater emphasis is given to compare the different impact of similar nanostructures on the TE performance of the *p*- and *n*-type Bi_2Te_3 nanocomposites. We finish this article by offering perspectives and outlook for the SE-MS–SPS technique.

Nanostructuring via MS–SPS process

Given the salient status of Bi_2Te_3 compounds in the field of TE research, there has been a consistent extensive effort of nanostructuring Bi_2Te_3 bulk materials over the past several years. There are a number of representative methods presented in the literature, ranging from hydrothermal synthesis followed by hot-pressing (HT-HP) [52, 53],

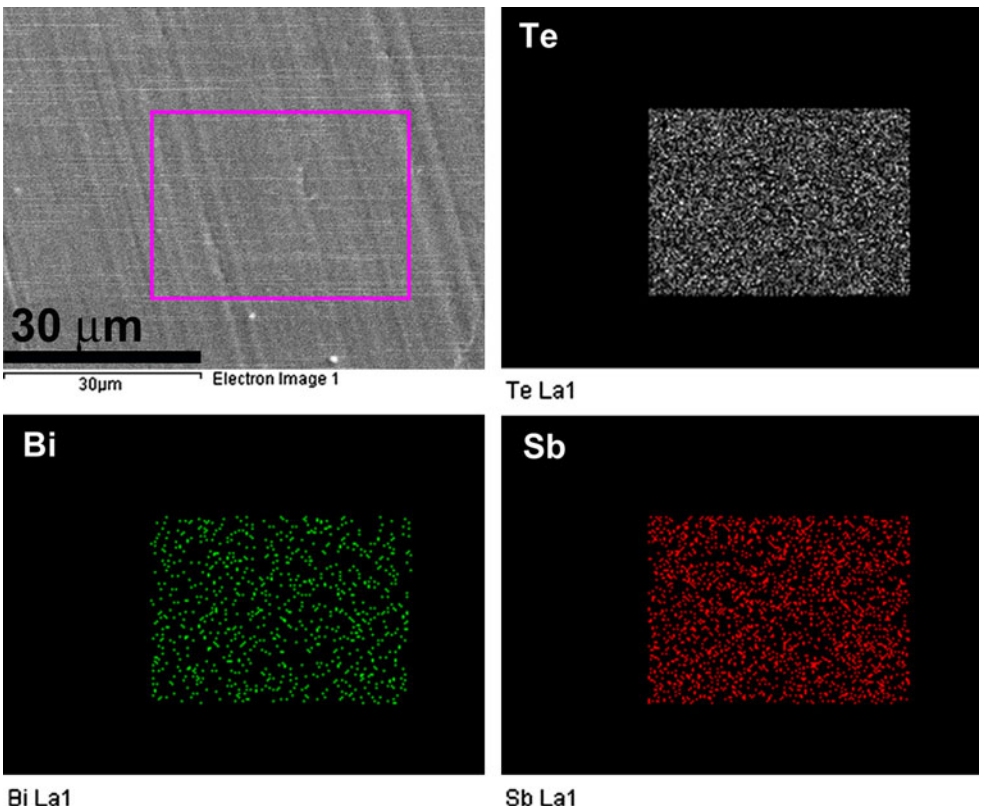

Fig. 6 EDS mapping results of CS for SE-MS-$Bi_{0.48}Sb_{1.52}Te_3$ ribbon

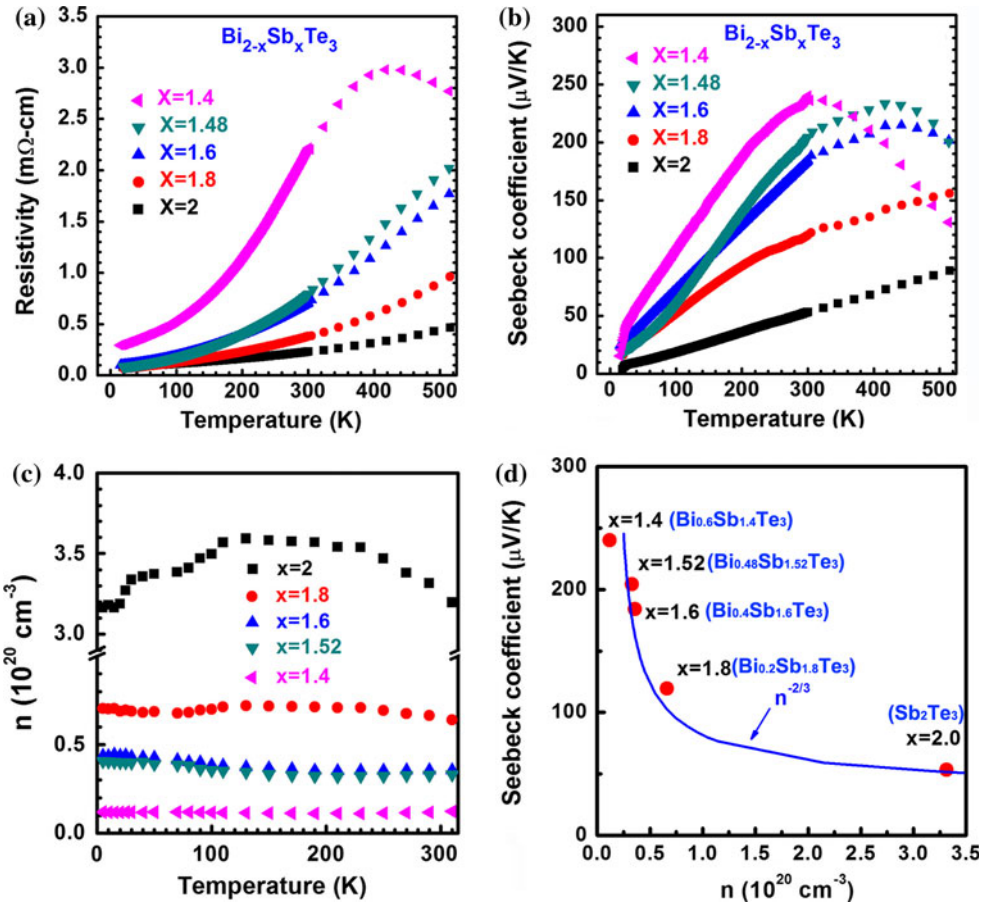

Fig. 7 **a** Resistivity, **b** Seebeck coefficient, and **c** carrier concentration of temperature dependence for SE-MS–SPSed $Bi_{2-x}Sb_xTe_3$ ($x = 1.4$–2.0) bulk samples. **d** The room temperature Seebeck coefficients as a function of carrier concentration and the solid line demonstrates such an $n^{-2/3}$ dependence

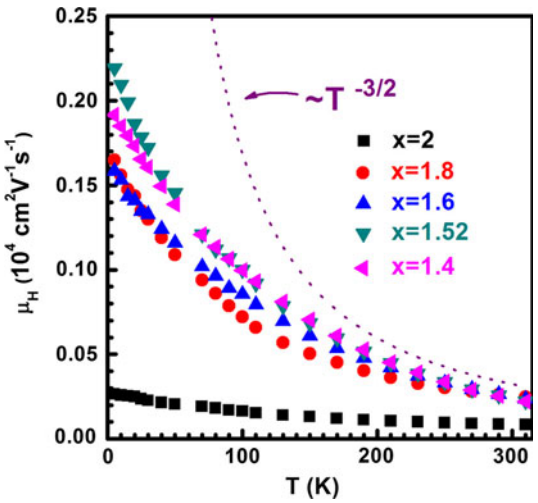

Fig. 8 The carrier mobility of temperature dependence for SE-MS–SPSed $Bi_{2-x}Sb_xTe_3$ ($x = 1.4$–2.0) bulk samples

evacuated-and-encapsulated sintering [63], ball-milling followed by hot-pressing (BM-HP) [54, 55, 64, 65], microwave synthesis followed by cold pressing and sintering [66], in situ strain-induced thermal forging technique [67, 68], to melt spinning followed by spark-plasma sintering (MS–SPS) [56–60, 62, 69–72]. The best *ZT* values of *p*-type $(Bi,Sb)_2Te_3$ nanocomposites reached 1.4–1.5 by using BM-HP [54, 55] or MS–SPS techniques [56–58]. Most of these methods are notably of two steps: generation of nanostructrures in/from the starting materials, followed by a densification process.

The commercial Bi_2Te_3 compounds, both *p*- and *n*-type, are prepared by a zone melting (ZM) method. A flow chart of a typical ZM process is illustrated in Fig. 1a. The elements are zone melted at 700 °C for 15 h and then annealed at 400 °C for ~36 h. The ZM condition must be finely controlled throughout the synthesis to ensure the quality of final product. Initially we used commercial ZM ingots as the starting materials [56, 57, 62, 72]. Due to the multi-scale microstructures induced by the MS–SPS process, the *ZT* of *p*-type ZM-MS–SPS $(Bi,Sb)_2Te_3$ nanocomposite was increased to ~1.5 at 300 K, an ~50 % improvement compared with that of the ZM ingot. However, the time and energy consuming ZM process was intact. It thus motivated our subsequent work on replacing the ZM ingots by single elemental Bi, Sb, Te, and Se powders. As a result, the total materials processing time has been shortened by an order of magnitude and the synthesis conditions are more tolerant. Figure 1b shows the more efficient SE-MS–SPS process.

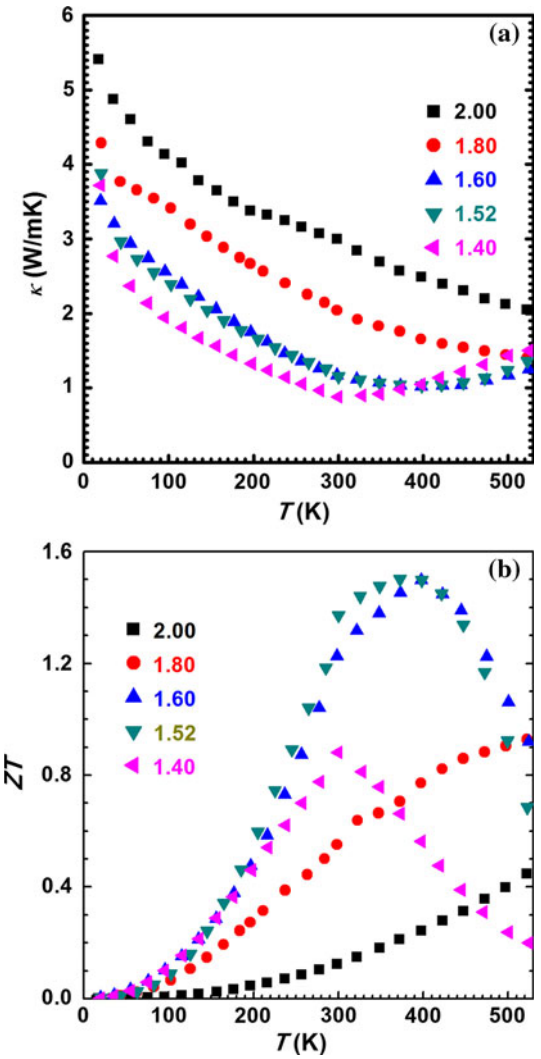

Fig. 9 **a** Thermal conductivity and **b** *ZT* values of temperature dependence for SE-MS–SPSed $Bi_{2-x}Sb_xTe_3$ ($x = 1.4$–2.0) bulk samples

MS and SPS processes

In this section, we briefly address the general technical features of the MS and SPS techniques. MS is a technique extensively used for preparing amorphous materials via quenching metal melts; the cooling rate is as high as 10^4–10^7 K/s depending on detailed processing parameters and materials [73–75]. During the MS process, a thin stream of metal melts and then is dripped onto a rapidly rotating copper wheel that is internally water cooled. Due to the exceptionally high thermal conductivity of cooper, the heat of metal melts is transferred to copper wheel at a high rate to incur amorphorizaion of the melts, typically yielding melt spun ribbons. Figure 2a, b shows the picture of melt spinner system we used and the as-obtained Bi_2Te_3 ribbons from the MS process, respectively. As shown in Fig. 2b, the Bi_2Te_3 ribbons are typically 1–3 mm wide, 7–40 μm thick, and several cm in length. Higher rotating speed results in thinner and narrower ribbons. For convenience, we hereafter call the surface of ribbon that comes into direct contact the copper wheel as the contact surface (CS), and the other surface as the free surface (FS). Figure 2c shows the CS (convex) and the FS (concave) of ribbon.

The melt-spun ribbons are hand ground into powders in air, and consolidated into dense pellets using a SPS method. In a typical SPS process, the powders are placed in a graphite die and a small uniaxial pressure is applied via two graphite rods, and then a large pulsed DC current is injected into the sample, giving rise to Joule heating, current/field assisted/enhanced mass transport, momentary spark discharge, or spark-plasma heats. These physical mechanisms in the SPS process allows for a greater control of micro-morphology while achieving high and uniform densification at a lower sintering temperature in a shorter period of time (minutes) than other sintering processes. The detailed SE-MS–SPS procedure is illustrated in Fig. 3.

SE-MS–SPSed *p*-type $(Bi,Sb)_2Te_3$ nanocomposites

This section is devoted to the detailed preparation procedure of SE-MS–SPSed *p*-type $(Bi,Sb)_2Te_3$, and discussions on how the nanostructures impact their TE performance.

Preparation and TE properties

High purity single elemental chunks of Bi (5*N*), Sb (6*N*), and Te (6*N*) were weighed according to the stoichiometry of $Bi_{2-x}Sb_xTe_3$ ($x = 0.0$–2.0) and cold pressed by hydraulic press with a pressure of 110 MPa. Excess Te (3–5 at.%) is added to compensate its volatilization during the MS processes. The pressed pieces were loaded in a quartz tube with a 0.5 mm diameter nozzle, purged with argon, inductively melted, and ejected under a pressure of 0.06 MPa Ar onto the copper wheel rotating with a linear speed of 40 m/s. The obtained ribbons were hand ground and then sintered by the SPS method at 773 K for 1 min (total SPS time is 5 min) with a pressure of 15 MPa to obtain the compact $Bi_{2-x}Sb_xTe_3$ ($x = 0.0$–2.0) pellet samples.

The phase compositions were inspected by powder X-ray diffraction (PXRD) at each step. All XRD peaks can be indexed to a rhombohedral lattice and no secondary phases were detected (Fig. 4a). The XRD peaks show a systematic shift to higher angle with increasing nominal Sb content, indicating Sb substitution in the crystal lattice and thus the formation of solid solutions. In particular, the shift of (125) peak is highlighted in Fig. 4b.

Despite the high cooling rate in the MS process, Bi_2Te_3 compounds, solid or liquid, have relatively low thermal

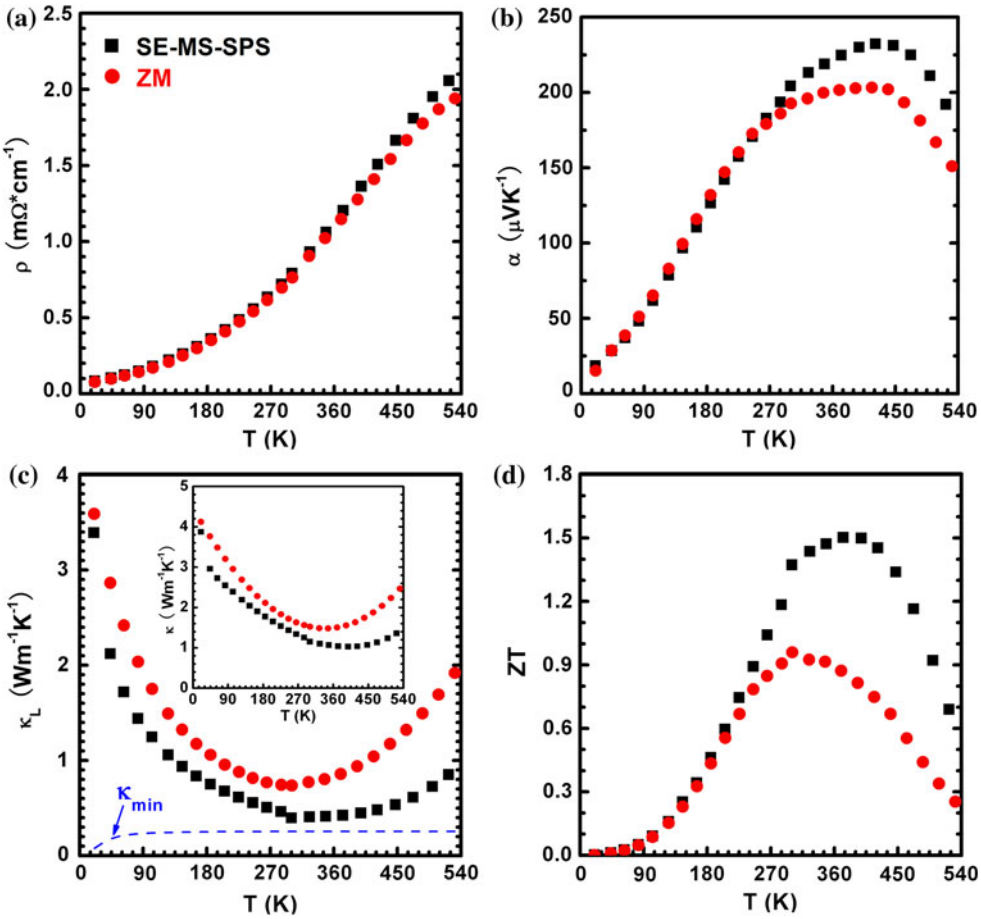

Fig. 10 Thermoelectric properties of ZM ingot and SE-MS–SPSed $Bi_{0.48}Sb_{1.52}Te_3$ nanocomposite: **a** electrical resistivity; **b** Seebeck coefficient; **c** lattice thermal conductivity inserted by total thermal conductivity; **d** figure of merit *ZT* values. Carrier thermal conductivity κ_e is estimated by the Wiedemann–Franz relation, $\kappa_e = LT/\rho$, and the Lorenz number $L = 2.0 \times 10^{-8}$ V^2/K^2 for a heavily doped semiconductor. The same Lorenz number (2.0×10^{-8} V^2/K^2) is used to estimate the κ_e of ZM ingot and SE-MS–SPSed nanocomposite. Reproduced with permission from Ref. [58]. Copyright 2010, American Chemical Society

conductivity, so complete amorphorization of melts is hard to achieve. Instead, a gradual microstructure changeover is formed between the CS and the FS due to the temperature gradient and thus different nucleation processes at different positions within ribbon. Figure 5 presents the field emission scanning electron microscopy (FESEM) images of the microstructures of $Bi_{2-x}Sb_xTe_3$ ($x = 0.0$–2.0) ribbons. While the FS exhibits interconnected dendritic crystals of 200–500 nm wide (Fig. 5a), we do not observe any discernible microstructures on the CS (Fig. 5b). The results of energy-dispersive X-ray spectroscopy (EDS) study shows that the composition on the CS and the FS is slightly different, as summarized in Table 1. Such compositional difference is attributed to different diffusion constant of Bi, Sb, and Te atoms during quenching. Nonetheless, the results of EDS mapping confirm that the composition is homogeneous on a micrometer length scale on the CS and the FS, respectively (Fig. 6). After the SPS process, the composition is homogeneous on an micrometer length scale throughout the pellet sample.

We find that the type of conduction (i.e., the sign of the Seebeck coefficient, Fig. 7b) is directly governed by the Sb-doping ratio. The SE-MS–SPSed $Bi_{2-x}Sb_xTe_3$ nanocomposites exhibit *n*- and *p*-type behavior at $0 \le x \le 1.2$ and $1.4 \le x \le 2$, respectively. We will focus on the *p*-type behavior in accordance with the theme of this section. As shown in Fig. 7a, ρ of SE-MS–SPSed $Bi_{2-x}Sb_xTe_3$ ($x = 1.4$–2.0) decreases rapidly with increasing x in the entire temperature range studied. The room temperature ρ of $Bi_{0.6}Sb_{1.4}Te_3$ is ~ 2.2 mΩcm, almost ten times as high as that of Sb_2Te_3. As shown in Fig. 7b, α exhibits a pronounced peak, indicating the onset of bipolar conduction (minority carriers of opposite sign are being excited into the conduction band). The peak position notably shifts to higher temperature with the increase in x. The systematic changes in the XRD peaks, ρ, and α with varying x corroborate the modification of band structure by Sb-doping. This is further confirmed by the x-dependence of the carrier concentration, n (Fig. 7c): n increases remarkably with x. To understand the mechanism underlying the x-dependence variation of α, by assuming a degenerate semiconductor approximation, we express α in a single parabolic band model as [76]:

$$\alpha = (1+\lambda)\frac{8\pi^2 k_B^2 T m^*}{3eh^2}\left(\frac{\pi}{3n}\right)^{2/3} \quad (1)$$

where λ, k_B, E_F, h, n, and m^* are the carrier scattering parameter, Boltzmann constant, Fermi energy, Planck constant, hole concentration (*p*-type conduction), and hole

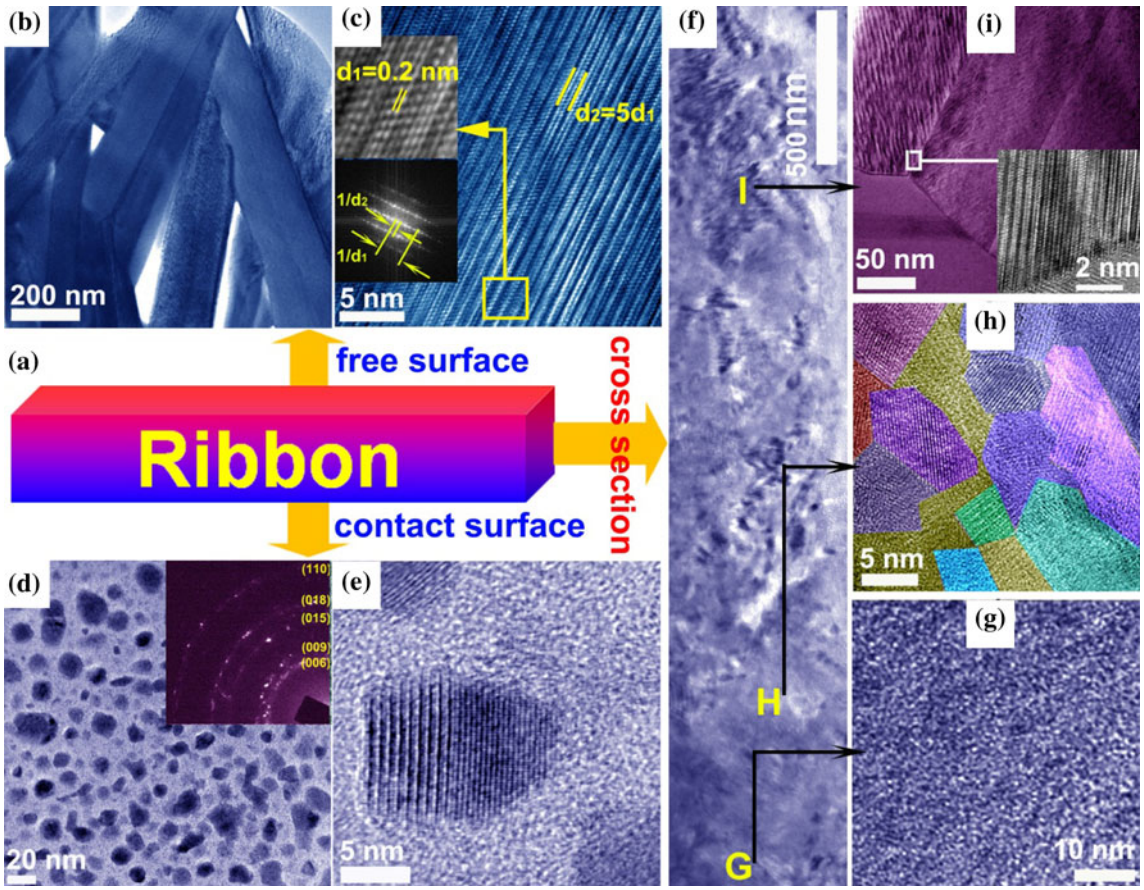

Fig. 11 **a** Schematic of melt-spun ribbon; **b** TEM image of free surface that is featured by micro-size dendritic crystals, and **c** HRTEM image of nanoscale modulation in the dendritic crystal shown in (**b**); **d** TEM image of near contact surface, and **e** HRTEM image of nanocrystalline domains near contact surface; **f** TEM image of the cross-section of ribbon, *bottom* and *up* of figure (**f**) are near the contact surface and free surface, respectively. **g** HRTEM image of amorphous phase near contact surface, **h** HRTEM image of nanocrystalline domains with mostly coherent boundary, **i** TEM image of micro-size crystals, and the *inset* is the HRTEM image of the nanoscale modulation. Reproduced with permission from Ref. [58]. Copyright 2010, American Chemical Society

effective mass, respectively. It should be noted that the system can be treated as single band near room temperature where the bipolar effect is small. The relationship of room temperature α–n is presented in Fig. 7d and the solid line demonstrates an $n^{-2/3}$ dependence (Pisarenko plot) as expected from a dominant acoustic phonon scattering of charge carriers. The temperature dependence of mobility also confirmed that acoustic phonon scattering is the main scattering mechanism near the room temperature, as shown in Fig. 8. It is thus concluded that the change in α is influenced primarily by the variation of n rather than the change of scattering mechanism.

The κ and ZT of the SE-MS–SPSed $Bi_{2-x}Sb_xTe_3$ ($x = 1.4$–2.0) nanocomposites are shown in Fig. 9 as a function of T. As displayed in Fig. 9a, κ increases with increasing x. This is understandable that Sb-substitution increases n and thus σ, leading to an enhanced κ_e according to the Wiedemann–Franz relationship. Moreover, the deviation of Sb/Bi ratio from the ratio of 1:1 would presumably weaken the phonon scattering induced by short-range mass and strain field fluctuation, resulting in an increased κ_L. Due to the low κ and high α, the ZT of SE-MS–SPSed $Bi_{0.48}Sb_{1.52}Te_3$ and $Bi_{0.4}Sb_{1.6}Te_3$ nanocomposites reach $\sim$1.5 at 390 K (Fig. 9b). Hence, we successfully replace the ZM ingots with single elements and making the SE-MS–SPS procedure time and energy efficient without sacrificing the TE performance.

The origin of ZT improvement for SE-MS–SPSed $Bi_{0.48}Sb_{1.52}Te_3$ nanocomposite

Now we discuss the origin of ZT improvement in the SE-MS–SPS sample. First, let us compare the TE properties of SE-MS–SPSed $Bi_{0.48}Sb_{1.52}Te_3$ and the commercial ZM ingot with the same composition in Fig. 10. While both samples have a similar n on the order of 3×10^{19} cm^{-3} within $\pm$10 % of each other, the slightly higher ρ, moderately enhanced α, and significantly reduced κ lead to a ZT

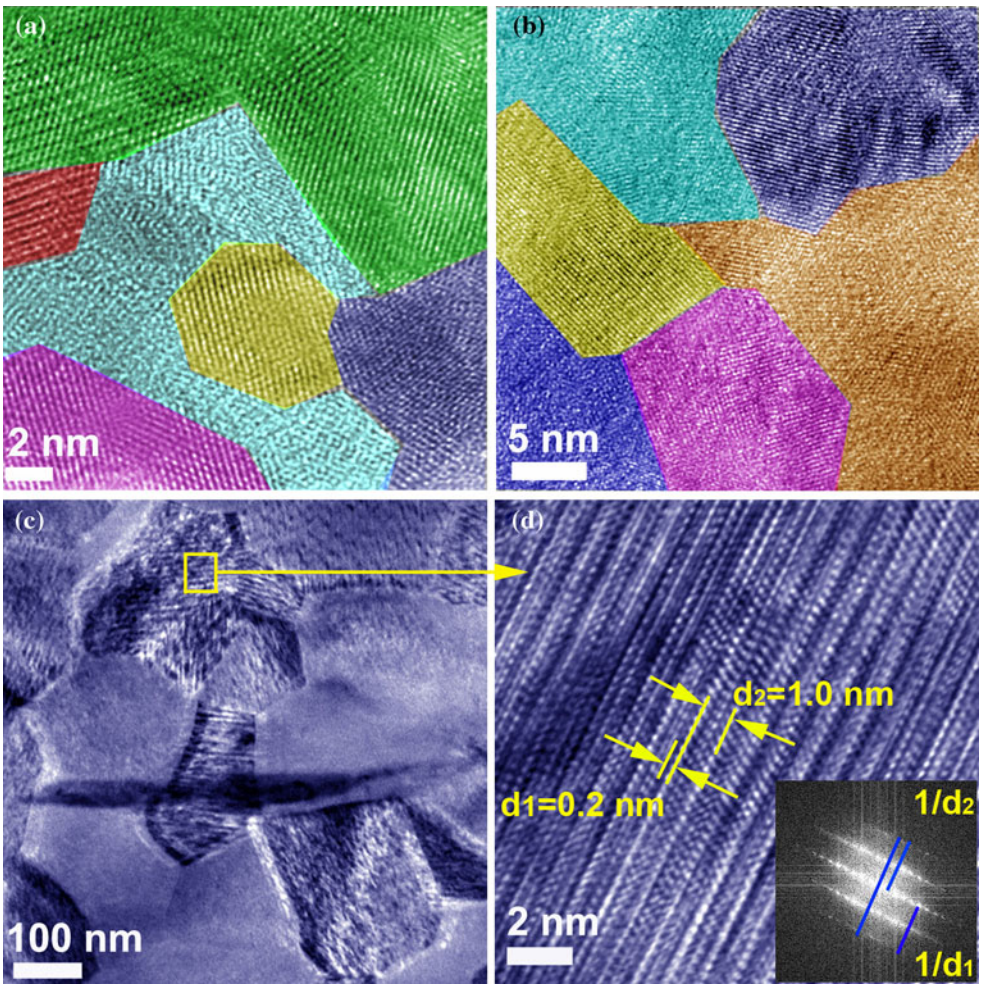

Fig. 12 **a**, **b** HRTEM images of typical microstructures contained 10–20 nm nanocrystals embedded in the bulk matrix. **c**, **d** HRTEM images of nanoscale modulations. Reproduced with permission from Ref. [58]. Copyright 2010, American Chemical Society

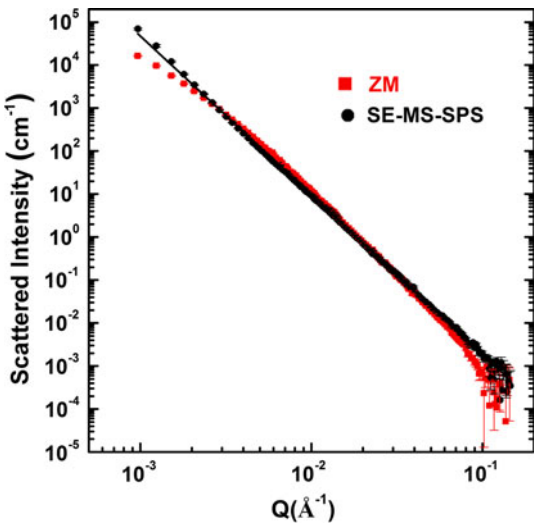

Fig. 13 SANS intensities as a function of momentum transfer Q in a *double-logarithmic* plot. The SE-MS–SPS sample is fitted with a Q^{-a} in all Q range with $a = 3.7$ (*black line*). Reproduced with permission from Ref. [58]. Copyright 2010, American Chemical Society

enhancement of ~50 % or more in SE-MS–SPSed $Bi_{0.48}Sb_{1.52}Te_3$ between 280 and 540 K as compared with that of the ZM ingot. Both the ZM ingot and SE-MS–SPSed nanocomposite exhibit typical semimetallic behavior in electrical resistivity and Seebeck coefficient. Despite the similar resistivity behavior, they display a different Seebeck behavior in several important aspects. The SE-MS–SPSed nanocomposite has as much as 10 % higher Seebeck value than the ZM ingot between 270 and 540 K. Furthermore, the Seebeck coefficient of SE-MS–SPSed nanocomposite peaks at $T \approx 450$ K, significantly higher than that of the ZM ingot. The results of Hall coefficient measurements indicated that both samples have a carrier concentration on the order of 10^{19} cm^{-3} and within ±10 % of each other between 5 and 300 K. Furthermore, the $T^{-3/2}$ dependence of Hall mobility is consistent with a predominant electron–phonon scattering near room temperature. The concomitant enhancement and the upshift of the Seebeck coefficient peak with temperature strongly suggest that the nanostructuring process induced a favorable change in the Fermi surface

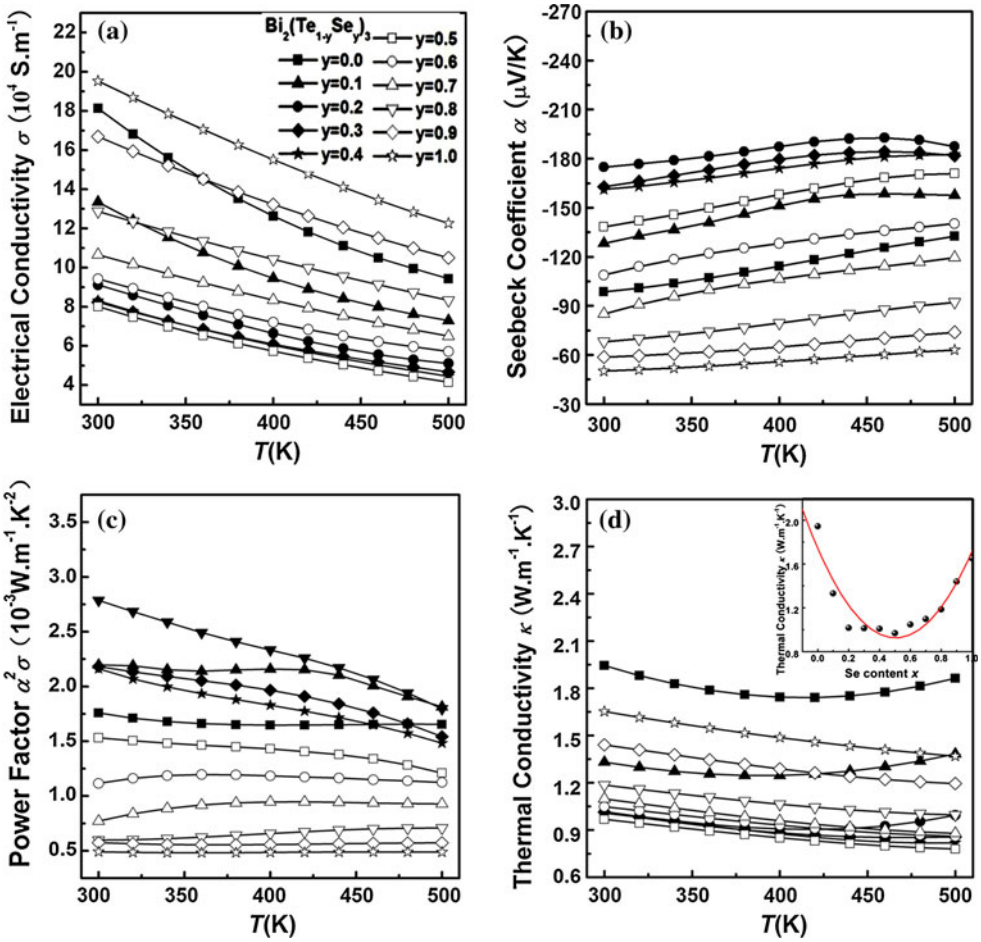

Fig. 14 Thermoelectric properties of SE-MS–SPSed $Bi_2(Te_{1-y}Se_y)_3$ nanocomposite: **a** electrical conductivity; **b** Seebeck coefficient; **c** power factor; **d** thermal conductivity. The *inset* in (**a**) shows the composition dependence of thermal conductivity at room temperature. Reproduced with permission from Ref. [60]. Copyright 2011, Elsevier

topology. This argument is further supported by the temperature dependence of the lattice thermal conductivity. As shown in the main panel and inset of Fig. 10c, the minima of lattice thermal conductivity (κ_L) and total thermal conductivity (κ) are close to the temperature where the Seebeck coefficient peaks, a signature of bipolar thermal conduction. The MS–SPS nanostructuring procedure thus alters the band structure and shifts the impact of the detrimental bipolar effects to higher temperatures. The similar result is also reported in ball-milled BiSbTe nanocomposites [54]. Excluding the contributions from textures and crystal chemistry, we conclude that the *ZT* enhancement arises from the specific microstructures generated in the MS–SPS procedure. In the following, we will inspect closely the microstructures of the melt-spun ribbon and the microstructures of the spark-plasma sintered pellet.

The microstructures of $Bi_{0.48}Sb_{1.52}Te_3$ ribbon are shown in Fig. 11. Apparently multiple length scale microstructures are formed between the CS and the FS of ribbon, ranging from the amorphous phase near the CS (Fig. 11g), 5–10 nm nanocrystallines embedded in amorphous matrix in the interior (Fig. 11h), to 200–500 nm wide dendrites with nanoscale modulations near the FS (Fig. 11i). These microstructures are further refined in the SPS process. As shown in Fig. 12a, b, we observe numerous of 10–20 nm nanocrystals in the SE-MS–SPSed $Bi_{0.48}Sb_{1.52}Te_3$ sample by HRTEM. It is also worth noting that the grain boundaries between nanocrystals are nearly coherent. The results of small angle neutron scattering (SANS) corroborate the evolution of microstructures in the MS and SPS processes and the nearly coherent grain boundaries. As shown in Fig. 13, a salient power-law behavior of the SANS intensity ($I \sim Q^{-a}$) for the SE-MS–SPSed $Bi_{0.48}Sb_{1.52}Te_3$ nanocomposite from $Q_{min} = 0.001$ to $Q_{max} = 0.1$ Å^{-1} indicates that the existence of a broad distribution of microstructures over a decade or more in length scale; and the power exponent $a = 3.70 \pm 0.01$ is close to 4, indicating that the grain boundaries are nearly coherent according to the Porod's theory [77, 78]. The results of microscopy study and neutron scattering agree well with each other. Very importantly, the nanocrystals with nearly coherent grain boundaries are not observed in the commercial ingot sample, so we conclude they are the key nanostructures responsible for the reduced lattice thermal

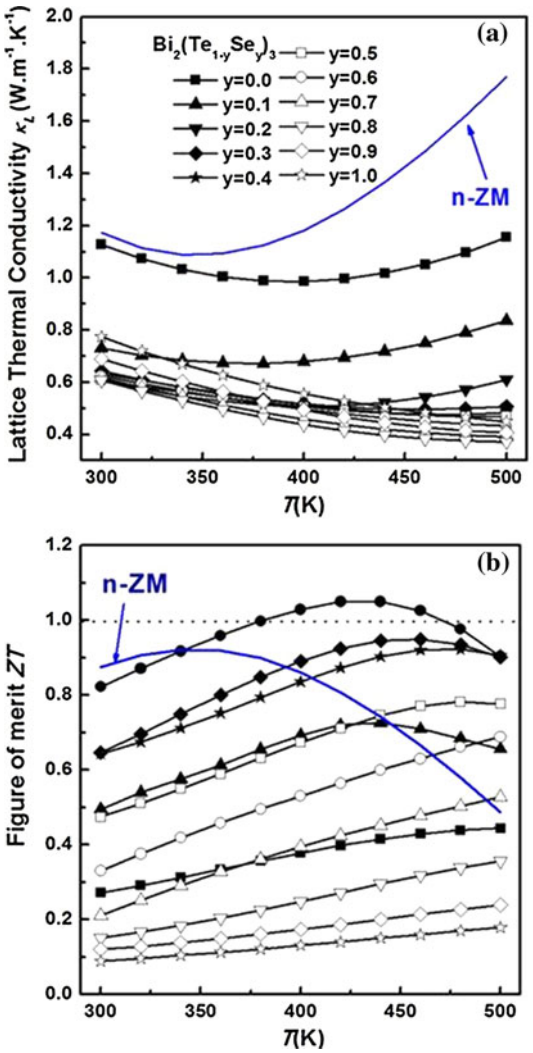

Fig. 15 **a** Lattice thermal conductivity and **b** the ZT values of temperature dependence for SE-MS–SPSed $Bi_2(Se_yTe_{1-y})_3$ nanocomposite. Reproduced with permission from Ref. [60]. Copyright 2011, Elsevier

conductivity and the enhanced *ZT*. We note that similar nanostructures were reported in the high performance BM-HPed *p*-type Bi_2Te_3 nanocrystalline bulk materials [54, 55].

The significant gain in the *ZT* via nanostructuring $Bi_{0.48}Sb_{1.52}Te_3$ come primarily the reduction of κ_L, irrespective of the detailed preparation methods. The SE-MS–SPSed sample possesses a $\kappa_L \sim 0.4$–0.5 W/m–K in the temperature range of 300–400 K, close to the alloy limit, in comparsion to a $\kappa_L \sim 0.8$–0.9 W/m–K of the ZM ingot [58]. The results of inelastic neutron scattering show that the generalized phonon density of states (GDOS) for the SE-MS–SPSed sample and the ZM ingot are practically the same, so they should have identical velocity of sound and heat capacity. In view of the phenomenological relation, $\kappa_L \sim C_v < v > l_{ph}$, where C_v is the specific heat per volume, $<v>$ the velocity of sound, l_{ph} the phonon mean-free path, the observed difference in the κ_L must be due to the difference in the l_{ph}. With known κ_L, C_v, and $<v>$ values, we estimate that the l_{ph} is on the order of 1–10 nm. Since all phonon modes contribute to the C_v but not all phonon modes contribute to the κ_L, the value of 1–10 nm is more of a lower limit of the l_{ph}, which is close to the average size of nanocrystals. Note that the nanostructuring process has a fairly small affect on the ρ (Fig. 9a), we conclude that the nearly coherent grain boundaries scatter the heat-carrying phonons more effectively than the charge carriers.

SE-MS–SPSed *n*-type $Bi_2(SeTe)_3$ nanocomposite

A TE device is comprised of two legs each made of *n*- and *p*-type materials. The TE performance and the mechanical properties of the *n*- and *p*-type materials should be as close as possible in order to maximize the output and insure the best mechanical robustness of the device [79]. In view of the successful implementation of the MS–SPS and BM-HP techniques in the *p*-type Bi_2Te_3 (SE-MS–SPSed *p*-type $(Bi,Sb)_2Te_3$ nanocomposites, section), it is instructive to implement the same nanostructuirng procedure in the *n*-type Bi_2Te_3. Interestingly, the *ZT* improvement of the *n*-type material turned out to be small [59, 60, 70, 71, 80, 81]. We will discuss this discrepancy and possible solution in the section "Why the MS–SPS procedure is less effective in *n*-type $Bi_2(SeTe)_3$ nanocomposites".

Preparation and TE properties

$Bi_2(Te_{1-y}Se_y)_3$ (Se content $y = 0.0$–1.0) nanocomposites were prepared by the SE-MS–SPS procedure but with slightly adjusted processing conditions [60]. Figure 14 shows the TE properties of the SE-MS–SPSed $Bi_2(Te_{1-y}Se_y)_3$ samples as a function of *T*. The σ decreases monotonically with increasing *T*, typical of a degenerate semiconductor. Moreover, the magnitude of σ first decreases and then increases with increasing y, notably the *n* adopts a very similar trend of variation. We attribute the concomitant changes in σ and *n* to the co-variation in the anion–cation ratio and the density of point defects (including vacancies and antisite defects) [60]. As expected, the α exhibits an opposite trend in comparison to that of σ. The temperature dependences of power factors are presented in Fig. 14c, and the highest power factor reaches 2.8×10^{-3} Wm K^{-2} for the $Bi_2Te_{2.4}Se_{0.6}$ sample, which is much less than that of the *n*-type commercial ZM ingot ($\sim 5 \times 10^{-3}$ Wm K^{-2}) due to the significant loss in the α. As shown in Fig. 14d, the κ of low Se-content samples first decreases wit increasing *T* due to the U-process, and then increases because of the onset of bipolar conduction. The high Se-content samples, however, show a monotonic decreased κ with increasing *T*, mainly owing to the increased band-gap

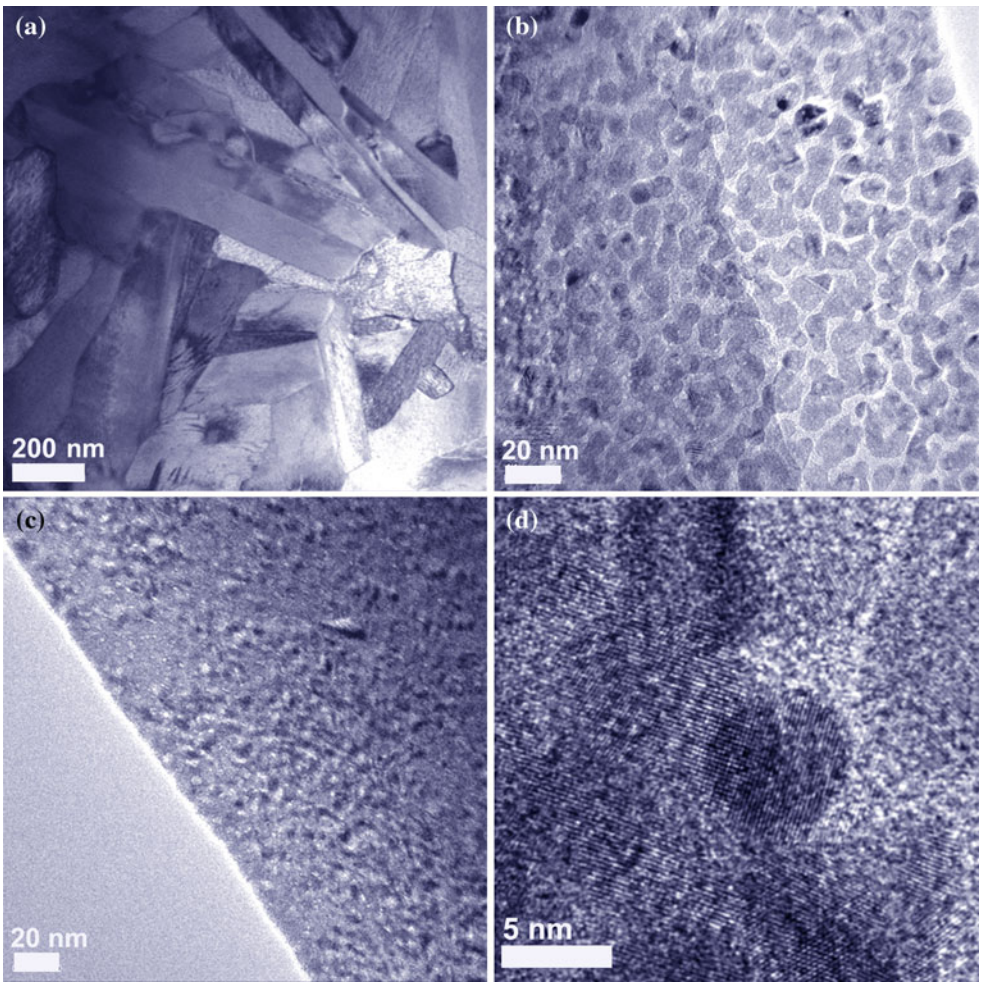

Fig. 16 The TEM images of SE-MSed n-type $Bi_2(Se_yTe_{1-y})_3$ ribbon. The TEM photos of **a** free surface that is featured by micro-size dendritic crystals, and **b** HRTEM image of contact surface with amorphous structures and numerous nanoinclusions; **c** the TEM image and **d** HRTEM image of the MS–SPS bulk samples with a mass of 5–10 nm nanoinclusions

that suppresses the intrinsic excitation. The κ_L shown in Fig. 15a is estimated by employing the Wiedemann–Franz relation, $\kappa_e = L\sigma T$, where the Lorenz number L is selected to be 1.5×10^{-8} V^2 K^{-2}. It is obvious that the SE-MS–SPS samples possess $\kappa_L \sim 0.6$–0.8 W/m K whereas the ZM ingot has ~0.8–1.2 W/m K at room temperature. The FESEM and HRTEM photos presented in Figs. 16 and 17 also show rich multi-scale nanostructures in *n*-type SE-MS–SPSed $Bi_2(Te_{1-y}Se_y)_3$ samples, similar to those identified in *p*-type counterparts (SE-MS–SPSed *p*-type $(Bi,Sb)_2Te_3$ nanocomposites, section). Hence it is plausible to attribute the reduced κ_L to the intensified phonon scattering by the multiple-scale nanostructures, and by the mass and strain-field fluctuations.

The *ZT* of the SE-MS–SPSed *n*-type $Bi_2(Se_yTe_{1-y})_3$ nanocomposites are plotted in Fig. 15b. With increasing Se-content, the *ZT* first increases and then fast decreases. The SE-MS–SPSed $Bi_2Te_{2.4}Se_{0.6}$ nanocomposite, due to its higher power factor and relatively low κ_L value, achieves the highest *ZT* value of 1.05 at 420 K, slightly improved over the *n*-type ZM ingot and consistent with previous reports [80, 81]. The *ZT* of SE-MS–SPSed $Bi_2Te_{2.4}Se_{0.6}$ nanocomposite possesses a weak temperature dependence and a relatively higher average *ZT* of 0.97 between 300 and 500 K, nonetheless, the nanostructuring-induced *ZT* improvement is limited compared to that of its *p*-type counterparts.

Why the MS–SPS procedure is less effective in *n*-type $Bi_2(SeTe)_3$ nanocomposites

It is instructive to note that the main contribution to the enhanced *ZT* in *p*-type Bi_2Te_3 nanocomposites is from the significant reduction of the κ_L and largely preserved σ underlain by "selective" grain boundary scattering. Similar nanostructures are formed in *n*-type material, but the outcome is somewhat disappointing: despite great efforts on optimizing chemical composition and MS–SPS conditions, the *ZT* can not exceed 1.1 mainly because of significant

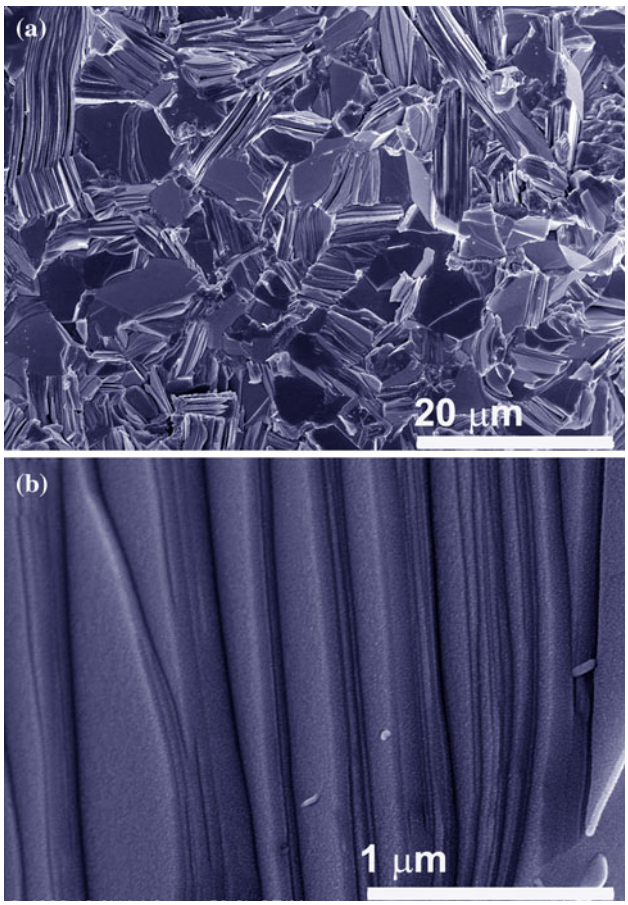

Fig. 17 The FESEM photos of the SE-MS–SPSed *n*-type $Bi_2(Se_yTe_{1-y})_3$ bulk samples, **a** low magnification image and **b** high magnification image

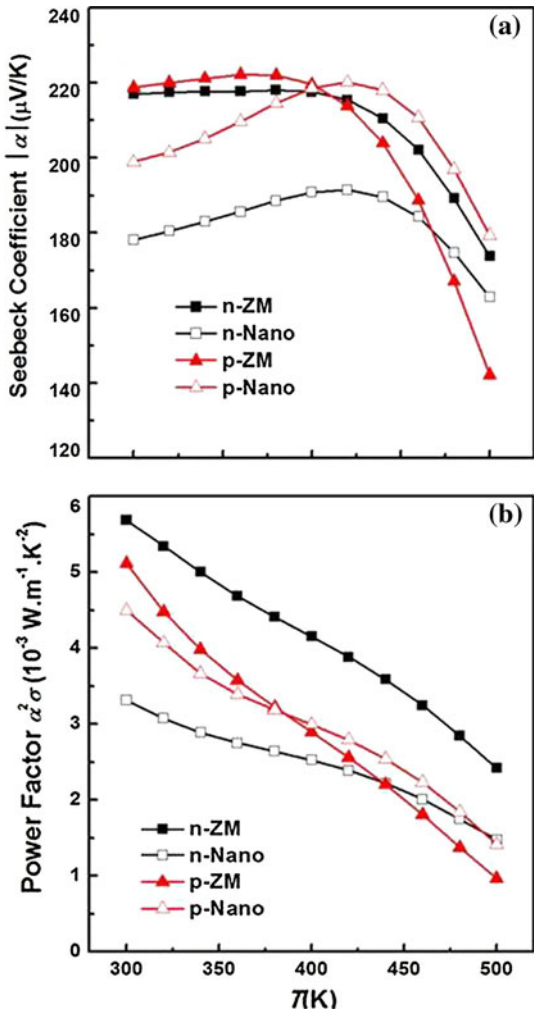

Fig. 18 **a** The Seebeck coefficients and **b** power factors of *p*- and *n*-type zone melting ingots (ZM) and ZM-MS–SPSed nanocomposites

decrease of α. Figure 18a shows the α of *p*-type and *n*-type ZM ingots and ZM-MS–SPSed sample with same composition and similar *n*. The α of ZM ingot is measured along the ZM growth directions. It is apparent that the *n*-type ZM-MS–SPSed sample shows a significantly lower α whereas the *p*-type ZM-MS–SPSed sample exhibits a comparable α, compare to their ZM counterparts. Due to the drop in α, the power factor for *n*-type ZM-MS–SPSed sample is severely degraded while there is not much change in the power factor of *p*-type material (Fig. 18b). Similar *n*, comparable σ and κ_L of *p*- and *n*-type ZM-MS–SPSed samples are in contrast to the large difference in α. The underlying mechanism of this observation is crucial for further optimizing the *n*-type Bi_2Te_3 material.

To this end, the first principles calculations by Huang and Kaviany [82] show the variation of α in two main crystallographic orientations as a function of chemical potential for both *p*- and *n*-type Bi_2Te_3 compounds (Fig. 19a). When $\mu-\mu_0 > 0$, the in-plane and cross-plane α are identical, and thus the α will be unchanged when the ZM ingots are crushed and nanostructured. Whereas when $\mu-\mu_0 < 0$, the magnitude of in-plane α is larger than that of out-of-plane α, in other words, the α is highly anisotropic in *n*-type Bi_2Te_3 material. In nanostructured materials, the magnitude of effective α is more of an averaged value over all orientations. Figure 19b shows the α of *n*-type ZM $Bi_2Te_{2.7}Se_{0.3}$ material experimentally measured in both in-plane and out-of-plane directions. It is apparent that the in-plane is higher than the out-of-plane counterpart, which is consistent with the calculated results of Huang et al. Because of the intrinsic anisotropic transport feature of electrons in *n*-type Bi_2Te_3 material, high anisotropy (texture) is necessary for preserving the electrical transport properties.

The *ZT* of *n*-type Bi_2Te_3 is susceptible to composition and texture: the highest *ZT* appears to be along the in-plane direction. If a *n*-type Bi_2Te_3 nanocomposite in which nanoinclusions have coherent boundaries/interfaces with the bulk matrix can be prepared, their κ_L shall be decreased while the electrical transport properties are preserved, a

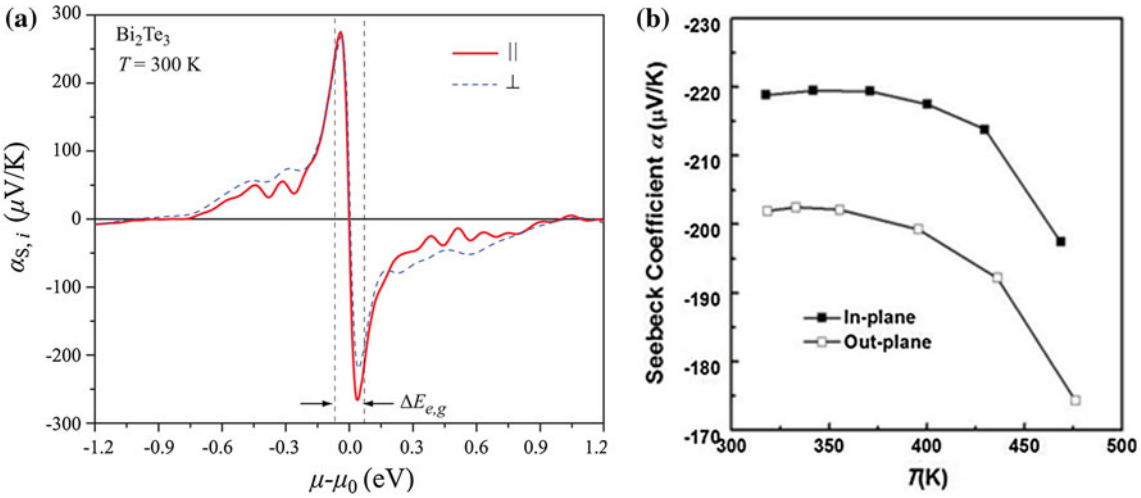

Fig. 19 **a** The variation of the calculated Seebeck coefficient of Bi_2Te_3 at $T = 300$ K with respect to the chemical potential (Reproduced with permission from Ref. [82]. Copyright 2008 by American Physical Society). **b** The measurement results for in-plane (ZM direction) and out-plane Seebeck coefficients of *n*-type $Bi_2Te_{2.7}Se_{0.3}$ ZM ingots

high *ZT* can be expected. To this end, polycrystalline materials with high anisotropy such as prepared by hot-extrusions or thermal forging would presumably show improved figure of merit and also reasonable mechanical properties.

Conclusions and outlook

Bi_2Te_3 is arguably the most widely used thermoelectric material. Higher performance Bi_2Te_3-based nanocomposite materials have been successfully produced using a unique nanostructuring approach: namely, single-element-melt-spinning spark-plasma sintering (SE-MS–SPS) procedure. Multiple scale microstructures generated by the MS process, in particular the 10–20 nm nanocrystals with nearly coherent grain boundaries, are believed (based on our SEM, TEM, and SANS experimental results) to account for the significant reduction of thermal conductivity without degrading the electrical transport properties of SE-MS–SPSed *p*-type $Bi_{0.48}Sb_{1.52}Te_3$ nanocomposite. As a result, more than 50 % enhancement in *ZT* is attained over a wide temperature range compared to the commercial zone melting material. Although the similar nanostructures are obtained in SE-MS–SPSed *n*-type $Bi_2(Se_xTe_{1-x})_3$ nanocomposites, and the lattice thermal conductivity is indeed reduced, the *ZT* does not significantly improve as much as it was expected because of the substantial degradation of the Seebeck coefficient. The degradation is attributed to the highly anisotropic nature of electrical transport properties in the *n*-type material. Hence, we propose several solutions to this challenge. Besides the *ZT* improvement in the SE-MS–SPSed nanocomposites, it is worth mentioned that the mechanical properties of nanocomposites are much superior to that of commercial ZM ingots. With regard to the material processing and module fabrications, the SE-MS–SPSed nanocomposites with significantly enhanced TE performance and mechanical properties have the great potential for near-term utilization commercial applications.

Both theoretical and experimental results prove that nanostructuring is a very effective route to improve *ZT* values for many traditional bulk thermoelectric materials. Moreover, some materials achieve the low limit lattice thermal conductivity via nanostructuring, and experimentally it is very hard to further decrease the lattice thermal conductivity. Therefore, the key and main goal in thermoelectric research is to further enhance *ZT* value via improving its power factor (especially the Seebeck coefficient). The main strategy to increase power factor is the "band structure engineering". Two noteworthy approaches are (1) distortion of the electronic density of states in Tl-doped PbTe [83, 84], and (2) convergence of electronic bands in Na-doped $PbTe_{1-x}Se_x$ [85]. However, these two approaches are not universal for all TE materials. More theoretical input is highly desirable in order to direct us toward new directions for improving the power factor.

Acknowledgments This study was supported by the International Science & Technology Cooperation Program of China (Grant No. 2011DFB60150), National Basic Research Program of China (Grant No. 2007CB607501), as well as 111 Project (Grant No. B07040). W. J. X would also like to thank the support by "the Fundamental Research Funds for the Central Universities" (Grant No. 2011-IV-112), Marie Curie Fellowship, and continued support and encouragement from Prof. Anke Weidenkaff and Dr. Sascha Populoh. J H. and T. M. T. would like to acknowledge the support by a DOE/EPSCoR Implementation Grant (#DE-FG02-04ER-46139) and the SC EPSCoR cost-sharing program.

References

1. Seebeck TJ (1823) Abhandlungen der Deutschen Akademie der Wissenschaften zu Berlin 1822–1823:265
2. Ioffe AF (1957) Semiconductor thermoelements and thermoelectric cooling. Infosearch Ltd., London
3. Slack GA (1995) In: Rowe DM (ed) CRC handbook of thermoelectrics. CRC Press, Boca Raton, p 407
4. Gordiakova GN, Sinani SS (1958) Sov Phys Tech Phys 3:908
5. Goldsmid HJ (1958) Proc Phys Soc 71:633
6. Goldsmid HJ, Sheard AR, Wright DA (1959) Br J Appl Phys 9:365
7. Ono T, Irie T, Taahama T (1962) J Phys Soc Jpn 17:1070
8. Efimova BA, Kolomoet LA (1964) Sov Phys Solid state 7:339
9. Evans DB, Mueller JJ (1964) IEEE Trans Aerospace 2:728
10. Steele MC, Rosi FD (1958) J Appl Phys 29:1517
11. Abrikoso NK, Zemskov VS, Iordanis EK, Petrov AV, Rozhdest VV (1969) Sov Phys Solid State 2:1468
12. Rowe DM, Bunce RW (1969) J Phys D Appl Phys 2:1497
13. Lidorenko NS, Dashevsky ZM, Dudkin LD, Skolozdra RV (1992) Dokl Akad Nauk SSSR 324:567
14. Poon SJ (2001) Semicond Semimet 70:37
15. Shen Q, Chen L, Goto T, Hirai T, Yang J, Meisner GP, Uher C (2001) Appl Phys Lett 79:4165
16. Culp SR, Poon SJ, Hickman N, Tritt TM, Blumm J (2006) Appl Phys Lett 88:042106
17. Cui Y, Zhu TJ, Shi RZ, Zhang Y, Zhao XB, He J (2009) Acta Mater 57:2757
18. Sales BC, Mandrus D, Chakoumakos BC, Keppens V, Thompson JR (1997) Phys Rev B 56:15081
19. Nolas GS, Morelli DT, Tritt TM (1999) Annu Rev Mater Sci 29:89
20. Tang XF, Chen LD, Goto T, Hirai T (2001) J Mater Res 16:837
21. Tang XF, Zhang QJ, Chen LD, Goto T, Hirai T (2005) J Appl Phys 97:093712
22. Shi X, Yang J, Salvador JR, Chi MF, Cho JY, Wang H, Bai SQ, Yang JH, Zhang WQ, Chen LD (2011) J Amer Chem Soc 133:7837
23. Snyder GJ, Christensen M, Nishibori E, Caillat T, Iversen BB (2004) Nat Mater 3:458
24. Brown SR, Kauzlarich SM, Gascoin F, Snyder GJ (2006) Chem Mater 18:1873
25. Gascoin F, Ottensmann S, Stark D, Haile SM, Snyder GJ (2005) Adv Func Mater 15:1860
26. Wang XJ, Tang MB, Chen HH, Yang XX, Zhao JT, Burkhardt U, Grin Y (2007) Appl Phys Lett 94:092106
27. Zevalkink A, Toberer ES, Zeier WG, Flage-Larsen E, Snyder GJ (2011) Eeergy Environ Sci 4:510
28. Nolas GS, Cohn JL, Slack GA, Schujman SB (1998) Appl Phys Lett 73:178
29. Martin J, Wang H, Nolas GS (2008) Appl Phys Lett 92:222110
30. Deng SK, Tang XF, Li P, Zhang QJ (2008) J Appl Phys 103:073503
31. Shi X, Yang J, Bai SQ, Yang JH, Wang H, Chi MF, Salvador JR, Zhang WQ, Chen LD, Wong-Ng W (2010) Adv Func Mater 20:755
32. Scherrer H, Scherrer S (1995) In: Rowe DM (ed) CRC handbook of thermoelectrics. CRC Press, Boca Raton, p 227
33. Hicks LD, Dresselhaus MS (1993) Phys Rev B 47:12727
34. Venkatasubramanian R, Siivola E, Colpitts T, O'Quinn B (2001) Nature 413:597
35. Hsu KF, Loo S, Guo F, Chen W, Dyck JS, Uher C, Hogan T, Polychroniadis TEK, Kanatzidis MG (2004) Science 303:818
36. Wang H, Li JF, Nan CW, Zhou M, Liu WS, Zhang BP, Kita T (2006) Appl Phys Lett 88:092104
37. Androulakis J, Hsu KF, Pcionek R, Kong H, Uher C, Dangelo JJ, Downey A, Hogan T, Kanatzidis MG (2006) Adv Mater 18:1170
38. Sootsman JR, Kong H, Uher C, D'Angelo JJ, Wu CI, Hogan TP, Caillat T, Kanatzidis MG (2008) Angew Chem Int Ed 47:8618
39. Li H, Tang XF, Su XL, Zhang QJ (2008) Appl Phys Lett 92:202114
40. Li H, Tang XF, Zhang QJ, Uher C (2008) Appl Phys Lett 93:252109
41. Li H, Tang XF, Zhang QJ, Uher C (2009) Appl Phys Lett 94:102114
42. Xiong Z, Chen XH, Huang XY, Bai SQ, Chen LD (2010) Acta Mater 58:3995
43. Xiong Z, Xi LL, Ding J, Chen XH, Huang XY, Gu H, Chen LD, Zhang WQ (2011) J Mater Res 26:1848
44. Chen LD, Huang XY, Zhou M, Shi X, Zhang WB (2006) J Appl Phys 99:064305
45. Xie WJ, He J, Zhu S, Su XL, Wang SY, Holgate T, Hubbard JW, Ponnambalam V, Poon SJ, Tang XF, Zhang QJ, Tritt TM (2010) Acta Mater 58:4705
46. Yu C, Zhu TJ, Xiao K, Shen JJ, Yang SH, Zhao XB (2010) J Electron Mater 39:2008
47. Yan XA, Joshi G, Liu WS, Lan YC, Wang H, Lee S, Simonson JW, Poon SJ, Tritt TM, Chen G, Ren ZF (2011) Nano Lett 11:556
48. Poon SJ, Wu D, Zhu S, Xie WJ, Tritt TM, Thomas P, Venkatasubramanian R (2011) J Mater Res 26:2795
49. Makongo JPA, Misra DK, Zhou XY, Pant A, Shabetai MR, Su XL, Uher C, Stokes KL, Poudeu PFP (2011) J Am Chem Soc 133:18843
50. Joshi G, Lee H, Lan YC, Wang XW, Zhu GH, Wang DZ, Gould RW, Cuff DC, Tang MY, Dresselhaus MS, Chen G, Ren ZF (2008) Nano Lett 8:4670
51. Yu B, Zebarjadi M, Wang H, Lukas K, Wang HZ, Wang DZ, Opeil C, Dresselhaus M, Chen G, Ren ZF (2012) Nano Lett 12:2077
52. Zhao XB, Ji XH, Zhang YH, Zhu TJ, Tu JP, Zhang XB (2005) Appl Phys Lett 86:062111
53. Cao YQ, Zhao XB, Zhu TJ, Zhang XB, Tu JP (2008) Appl Phys Lett 92:143106
54. Poudel B, Hao Q, Ma Y, Lan YC, Minnich A, Yu B, Yan XA, Wang DZ, Muto A, Vashaee D, Chen XY, Liu JM, Dresselhaus MS, Chen G, Ren ZF (2008) Science 320:634
55. Ma Y, Hao Q, Poudel B, Lan YC, Yu B, Wang DZ, Chen G, Ren ZF (2008) Nano Lett 8:2580
56. Xie WJ, Tang XF, Yan YG, Zhang QJ, Tritt TM (2009) Appl Phys Lett 94:102111
57. Xie WJ, Tang XF, Yan YG, Zhang QJ, Tritt TM (2009) J Appl Phys 105:113713
58. Xie WJ, He J, Kang HJ, Tang XF, Zhu S, Laver M, Wang SY, Copley JRD, Brown CM, Zhang QJ, Tritt TM (2010) Nano Lett 10:3283
59. Wang SY, Xie WJ, Li H, Tang XF (2010) J Phys D Appl Phys 43:335404
60. Wang SY, Xie WJ, Li H, Tang XF (2011) Intermatellics 19:1024
61. Zhang T, Zhang QS, Jiang J, Xiong Z, Chen JM, Zhang YL, Li W, Xu GJ (2011) Appl Phys Lett 98:022104
62. Tang XF, Xie WJ, Li H, Zhao WY, Zhang QJ, Niino M (2007) Appl Phys Lett 90:012102
63. Liu CJ, Lai HC, Liu YL, Chen LR (2012) J Mater Chem 22:4825
64. Lan YC, Minnich AJ, Chen G, Ren ZF (2010) Adv Func Mater 20:357
65. Lin SS, Liao CN (2011) J Appl Phys 110:093707
66. Mehta RJ, Zhang Y, Karthik C, Singh B, Siegel RW, Borca-Tasciuc T, Ramanath G (2012) Nat Mater 11:233
67. Shen JJ, Zhu TJ, Zhao XB, Zhang SN, Yang SH, Yin ZZ (2010) Energy Environ Sci 3:1519

68. Shen JJ, Yin ZZ, Yang SH, Yu C, Zhu TJ, Zhao XB (2011) J Electron Mater 40:1095
69. Xie WJ, He J, Zhu S, Holgate T, Wang SY, Tang XF, Zhang QJ, Tritt TM (2011) J Mater Res 26:1791
70. Wang SY, Xie WJ, Li H, Tang XF, Zhang QJ (2010) J Electron Mater 40:1150
71. Wang SY, Xie WJ, Li H, Tang XF (2010) Acta Phys Sin 59:8927
72. Wang SY, Xie WJ, Li H, Tang XF (2010) J Inorg Mater 25:609
73. Greer AL (1995) Science 267:1947
74. Tkatch VI, Denisenko SN, Beloshov ON (1997) Acta Mater 45:2821
75. Tkatch VI, Limanovskii AI, Denisenko SN, Rassolov SG (2002) Mater Sci Eng A 323:91
76. May AF, Snyder GJ (2012) Introduction to modeling thermoelectric transport at high temperature. In: Rowe DM (ed) Materials, preparation, and characterization in thermoelectrics. CRC Press, Boca Raton, p 11.1
77. Beaucage G (1995) J Appl Cryst 28:717
78. Beaucage G, Kammler HK, Pratsinis SE (2004) J Appl Cryst 37:523
79. Bottner H, Ebling DG, Jacquot A, Konig J, Kirste L, Schmidt J (2007) Phys Status Solidi: Rapid Res Lett 1:235
80. Yan XA, Poudel B, Ma Y, Liu WS, Joshi G, Wang H, Lan YC, Wang DZ, Chen G, Ren ZF (2010) Nano Lett 10:3373
81. Liu WS, Zhang QY, Lan YC, Chen S, Yan X, Zhang Q, Wang H, Wang DZ, Chen G, Ren ZF (2011) Adv Energy Mater 1:577
82. Huang BL, Kaviany M (2008) Phys Rev B 77:125209
83. Heremans JP, Jovovic V, Toberer ES, Saramat A, Kurosaki K, Charoenphakdee A, Yamanaka S, Snyder GJ (2008) Science 321:554
84. Heremans JP, Wiendlocha B, Chamoire AM (2012) Energy Environ Sci 5:5510
85. Pei YZ, Shi XY, LaLonde A, Wang H, Chen LD, Snyder GJ (2011) Nature 473:66